CHAPTER 16

# *Superconductivity in Nanostructured Boron-doped Diamond and its Application to Device Fabrication*

SOUMEN MANDAL,* TOBIAS BAUTZE AND CHRISTOPHER BÄUERLE*

Institut Néel, CNRS, Université Joseph Fourier, 38042, Grenoble, France
*Email: soumen.mandal@gmail.com; bauerle@grenoble.cnrs.fr

## 16.1 Introduction

Carbon, the material that all known life-forms contain, has plenty of allotropes. The most widely known among them are graphite, diamond and amorphous carbon. Diamond in particular has been known to mankind for almost 6000 years. Although the most common use of diamond is in jewellery, some of its extraordinary properties make it suitable for various engineering and scientific usages. It is one of the hardest materials known, which makes it an excellent candidate for cutting and grinding tools. In its pure form it is an insulator but it can be turned into a semiconductor or even a superconductor by sufficient doping. In nature, diamond is formed at high temperature and high pressure inside the earth at a depth of 140–190 km over a period of 1–3 billion years. It is also possible to grow diamond artificially by a high-pressure high-temperature process, which mimics the conditions present inside the earth.[1] Apart from this, chemical vapor

RSC Nanoscience & Nanotechnology No. 31
Nanodiamond
Edited by Oliver Williams

Published by the Royal Society of Chemistry, www.rsc.org

deposition (CVD) has also been used to grow diamond artificially.[2] The main advantage of this CVD process is the ability to grow diamond films on large substrates. It opens the possibility to use diamond in a variety of applications, like heat sinks for high heat-producing electronics, coatings to reduce wear and tear in mechanical tools, to name a few.[3] The CVD process also allows control of various other properties of the film. It is possible to grow films of varying grain sizes from a few nanometres to microns. Apart from this, one can add a variety of dopants to drastically change some of the properties of pure diamond. Naturally occurring blue diamond, which contains boron impurities, is semiconducting. The use of CVD has made it possible to alter the boron concentration such that doped diamond can even be turned superconducting. The first reported superconducting diamond was grown in 2004 by Ekimov *et al.*[4] using a high-pressure, high-temperature method. They achieved superconductivity by heavily doping the material with boron above a critical concentration. This discovery led to a flurry of activity in the study of superhard superconducting materials.[5–12] Diamond is now known to be a type-II superconductor with a critical temperature close to 4 K and a critical field in excess of 4 T.[4] However, recently, transition temperatures as high as 11 K have been achieved in homoepitaxial CVD-grown diamond films.[13]

The origin of superconductivity in diamond is still highly debated. At present there are three competing theories to explain its origin but any serious experimental evidence is missing to date. The three competing theories are: i) phonon mediated pairing-driven conventional BCS theory,[14] ii) correlated impurity band theory[15] and iii) weak localization of spin-flip-driven hole pairs close to the Fermi level.[16] Some recent studies on the isotopic shift of the transition temperature upon isotopic substitution of boron and carbon atoms point to conventional BCS theory,[17] but more experimental studies are required before a conclusion on the origin of superconductivity can be drawn.

Although the origin of superconductivity in diamond is an interesting field of study, our main interest lies in the fact that, in addition to its superconductivity, diamond also has a very high Young's modulus. This makes it an excellent candidate for making superconducting nano-electromechanical systems (NEMS) of very high quality. However, the realization of NEMS is only possible if it can be proven that the superconducting,[7–9] as well as the mechanical, properties[10] of the nanocrystalline layers of diamond grown on a non-diamond substrate, like silicon, are preserved even when the material is nanopatterned. This chapter will focus on a comprehensive study of nanopatterned superconducting diamond films grown on silicon dioxide on a silicon substrate. First, we will discuss the details of the nanofabrication process of diamond thin films. Then, we will present our results on low temperature studies of these nanopatterned circuits, followed by studies on diamond superconducting quantum interference devices (SQUIDs). We will conclude this chapter with the very first results on electromechanical systems made from boron-doped diamond.

## 16.2 Nanofabrication of Polycrystalline Boron-doped Diamond

Figure 16.1 shows the schematic of the complete nanofabrication process. We start with CVD-grown, boron-doped diamond on 500 nm thick silicon dioxide on a silicon substrate. The details of the growth process can be found elsewhere.[18–20] The film is thoroughly cleaned in mild acid solution followed by rinsing with water. Then, the film is dipped in acetone for a few minutes to remove further organic pollutants that may be present on the surface. As a final step, the sample is dipped in isopropyl alcohol, which is then allowed to evaporate to obtain a clean surface. This cleaned sample is spin coated with 4% polymethyl-methacrylate (PMMA) to form a 250 nm thick layer, which is then prebaked at 180 °C for 5 min. This layer of PMMA is exposed to an electron beam with a dose of $\sim$300 μC cm$^{-2}$ with an acceleration voltage of 20 kV. The exposed PMMA layer is then developed for 35 s in a solution of 1 : 3 methyl isobutyl ketone (MIBK) and isopropyl alcohol (IPA). The developed layer is then covered with 65 nm of nickel and evaporated in a standard electron-gun evaporator. This is followed by the lift-off process by dipping the sample in acetone, which results in a nickel pattern as shown in the middle panel of the second line in Figure 16.1. This nickel layer acts as a mask for the plasma etching process. The etching is done using an inductively coupled plasma-based reactive ion etching process. The sample is cooled to 10 °C while being exposed to the oxygen plasma for approximately 8 min. The anisotropic nature of the etching process results in structures with a height-to-width aspect ratio greater than three.

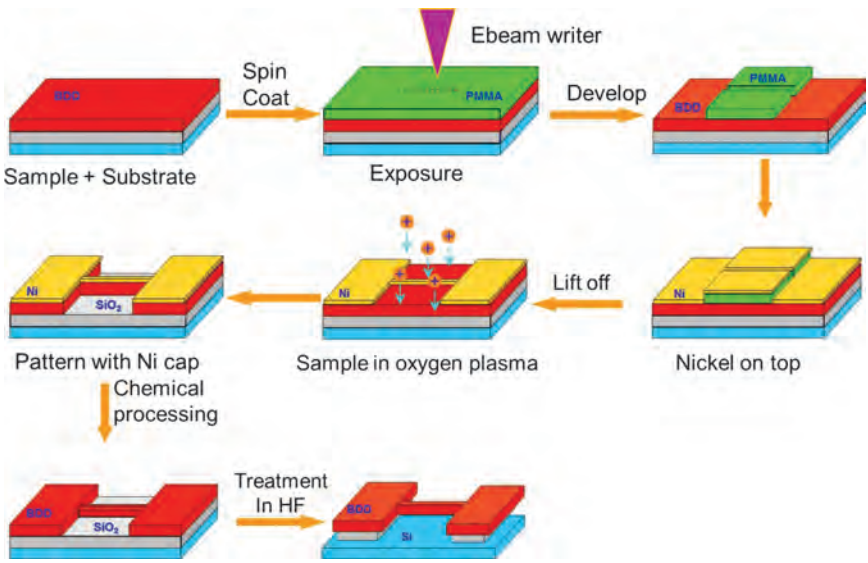


**Figure 16.1** Schematic of the nanofabrication process, starting from a diamond thin film to a nanomechanical system.

After this process, the nickel mask is removed by dipping the sample in $FeCl_3$ solution followed by cleaning in dilute acid solution, acetone and finally isopropyl alcohol. At this stage, ohmic contacts are evaporated on the contact pads using photolithography and a standard electron-gun evaporation technique. The ohmic contacts consist of a trilayer of titanium, platinum and gold with thicknesses of 30, 50 and 40 nm, respectively. This trilayer is then annealed in high vacuum at 750 °C for 30 min to form a titanium carbide interface between the metals and the diamond layer. This completes the process for realizing micro- and nano-circuits out of boron-doped diamond.

In Figure 16.2 we have shown scanning electron microscope (SEM) images of a typical circuit used for low-temperature characterization of nano-patterned diamond films. Note the small section in the last panel of the figure showing a line with a thickness of 350 nm, a length of 500 nm and a width of 90 nm. Such a high aspect ratio is possible due to the anisotropic nature of the etching process. In order to fabricate electromechanical systems, an additional step is added to this process, as shown in the last panel of Figure 16.1. The circuit is exposed to highly reactive hydrogen fluoride gas, which etches away the $SiO_2$ layer underneath the diamond, resulting in suspended structures of desired geometry. Diamond itself is inert to this chemical etching process. A typical suspended beam is shown in Figure 16.3.

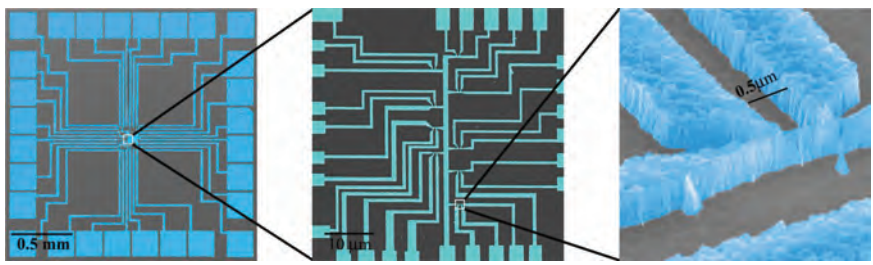


**Figure 16.2** A typical circuit made from boron-doped diamond using electron beam lithography techniques.
(Adapted with permission from Soumen Mandal *et al.* Nanostructures made from superconducting boron-doped diamond, *Nanotechnology*, 2010, **21**, 193503, IOP Publishing, UK.)

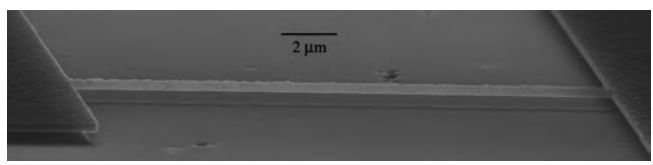


**Figure 16.3** A typical suspended beam fabricated out of boron-doped diamond.

## 16.3 Low-temperature Characterization of Nanofabricated Samples

In this section we will discuss the low temperature results for our nanofabricated circuits. The measurements were done using both standard DC and lock-in based AC measurement techniques in a common four-probe geometry. The measurements were performed in both $^3$He and $^3$He/$^4$He dilution refrigerators. For the electrical characterization of the film, silver paste contacts were deposited on the film within a distance of approximately 5 mm. The resistance was measured as a function of temperature with a bias current of 1 μA. The results are displayed in Figure 16.4. The transition temperature of the film was close to 3 K with a transition width of 0.7 K using 10–90% of the onset resistance criterion. The width in the transition temperature can be attributed to a variation of the grain sizes in the sample.

In Figure 16.5 we show the superconducting critical temperature $T_C$ of wires with various widths. For the measurements we used very low currents, typically of the order of 100 nA. The transition temperatures of the wires with widths greater than 100 nm are close to 2 K, which is similar to the bulk value of the wafer from which the circuit was fabricated. Only in the case of the narrowest wire, which is less than 100 nm wide, $T_C$ is close to 1.5 K.

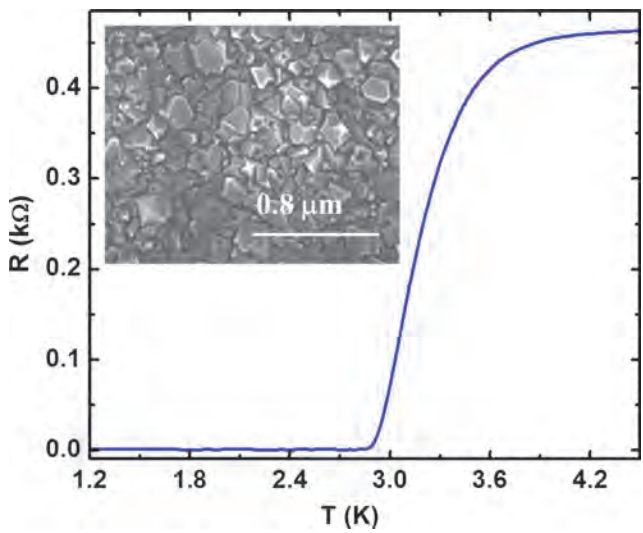


**Figure 16.4** Superconducting transition temperature of a boron-doped thin film. The inset shows the SEM image of the surface of an as-grown layer. The surface consists of grains with a typical size of 150 nm for a 250 nm thick film.
(Adapted with permission from Soumen Mandal *et al.* Nanostructures made from superconducting boron-doped diamond, *Nanotechnology*, 2010, **21**, 193503, IOP Publishing, UK.)

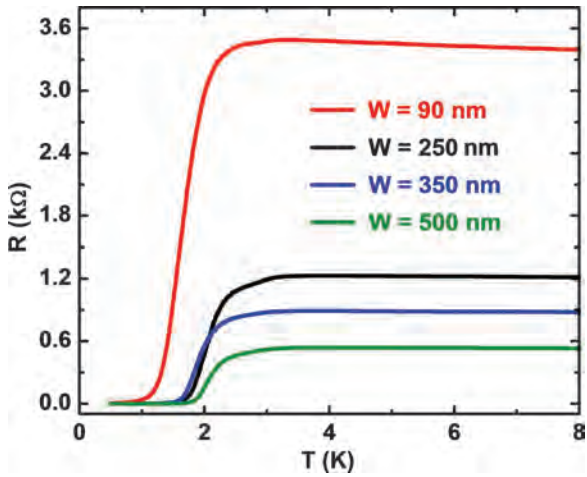


**Figure 16.5** Resistance *versus* temperature of four representative diamond wires of similar lengths and height with varying widths.
(Adapted with permission from Soumen Mandal *et al.* Nanostructures made from superconducting boron-doped diamond, *Nanotechnology*, 2010, **21**, 193503, IOP Publishing, UK.)

This observation is confirmed for other wafers, where wires with widths greater than 100 nm have $T_C$ values close to that of the non-patterned sample, while for wires thinner than 100 nm, a slight suppression of $T_C$ is seen. We have also measured the voltage–current ($V$–$I$) characteristics of these wires. Some of the results will be presented in this chapter, whereas detailed descriptions of the results can be found elsewhere.[21,22]

Figure 16.6 shows the $V$–$I$ curves measured on a 500 nm wide wire at various temperatures. The curves are hysteretic due to thermal effects. When the current in the wire is ramped up from zero, the voltage across the wire stays zero as long as the bias current is well below the critical current. Once the critical current is reached, the wire starts Joule heating due to its finite resistance. Subsequently, on decreasing the current, the critical current, usually called the re-trapping current, is much lower than what is measured while increasing the current.[23,24] The slight asymmetry of the $V$–$I$ curves is attributed to an offset in our measurement set-up. We have also done similar measurements at various temperatures on wires widths of 350, 250 and 90 nm.[22] The result for the 90 nm wire is shown in Figure 16.7.

The $V$–$I$ characteristic for the 90 nm wire is non-hysteretic even at temperatures as low as 50 mK. The critical current at the lowest temperature is close to 20 nA. The reason for the non-hysteretic nature of these curves is due to low power dissipation when the sample reaches the critical current. For a sample to show hysteretic behaviour, the power dissipated at the critical current must be higher than the re-trapping power of the sample. Here, the re-trapping power is close to 4.5 pW,[22] while the power dissipated at the critical current is of the order of 0.65 pW. Hence, in this case thermal

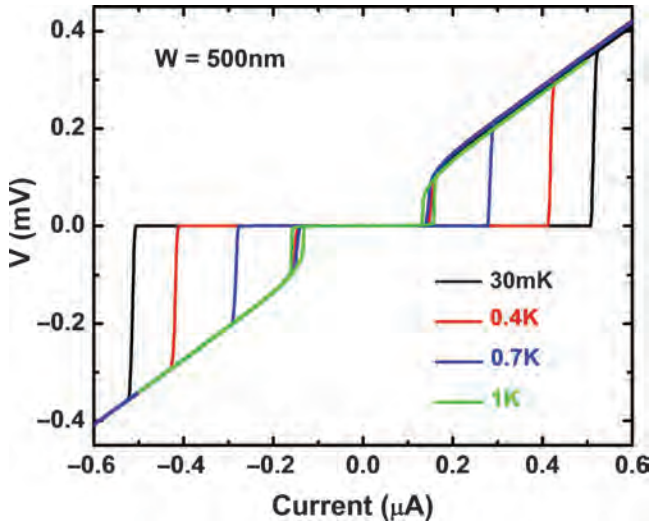


**Figure 16.6** Voltage–current (*V–I*) characteristics of a 500 nm wide wire taken at different temperatures. The characteristics are hysteretic due to Joule heating.
(Adapted with permission from Soumen Mandal *et al.* Nanostructures made from superconducting boron-doped diamond, *Nanotechnology*, 2010, **21**, 193503, IOP Publishing, UK.)

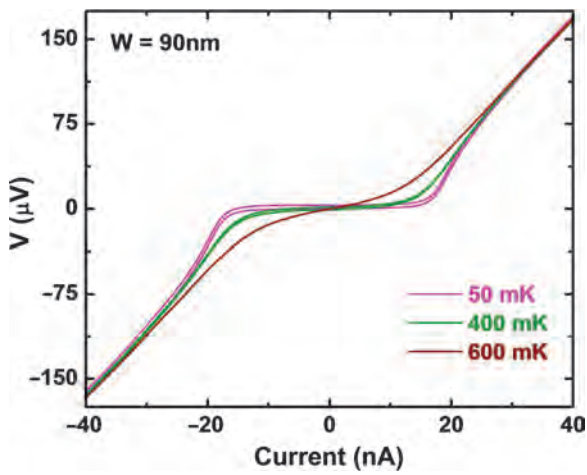


**Figure 16.7** Voltage–current characteristics at different temperatures for a wire with dimensions of 500 nm length, 90 nm width and 300 nm height. (Adapted with permission from Soumen Mandal *et al.* Detailed study of superconductivity in nanostructured nanocrystalline boron-doped diamond thin films, *Phys. Status Solidi A* 2010, **207** (9), 2017–2022, WILEY-VCH Verlag GmbH & Co. KGaA, Weinheim.)

effects do not come into play when the sample transits from the normal state to superconducting state and *vice versa.*

Apart from the temperature dependence of the *V–I* characteristics, we have also measured the isothermal *V–I* characteristics at various applied magnetic fields for in-plane, as well as out-of-plane, configurations. In Figure 16.8 we have presented the out-of-plane configuration results for a 500 nm wide wire. The curves are hysteretic until an applied field of 30 mT is reached.[21] Above 30 mT the curves are no longer hysteretic due to the fact that the critical current of the device is lower than the re-trapping current. The lowering of the critical current is because of the suppression of superconductivity due to magnetic field induced pair breaking effects. For a closer look at the data, we have numerically calculated the differential resistance of the sample, as presented in panel B of Figure 16.8. For fields as high as 500 mT, we have seen a clear zero resistance state close to zero injection current.[21] Above this field, even though the resistance never becomes completely zero, a local minimum at zero current suggests the existence of superconducting pockets, even at fields as high as 3 T. We have also measured the *V–I* characteristics of the wire by putting an in-plane field perpendicular to the flow of current. The results are shown in Figure 16.9.

In this case the curves are hysteretic until the in-plane applied field reaches a value of 130 mT, which is clearly different from what is seen in the case of the out-of-plane applied field. One quick look at the curves in panel A of Figures 16.8 and 16.9 tells us that, for the same applied field, the critical current is higher for the case when the applied field is in the plane of the sample. We believe that the suppression of the critical current in this system

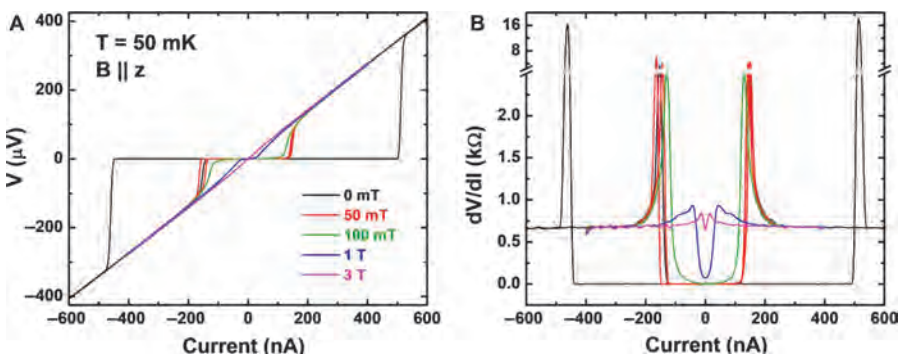


**Figure 16.8** Isothermal ($T = 50$ mK) voltage–current characteristics of a 500 nm wide wire taken at various applied magnetic fields. The field is perpendicular to the sample. The *V–I* characteristics are hysteretic below 30 mT. In panel B we have shown the differential resistance extracted numerically from the *V–I* curves. The resistance goes to zero when the wire is in its superconducting state.
(Adapted with permission from Soumen Mandal *et al.* Nanostructures made from superconducting boron-doped diamond, *Nanotechnology*, 2010, **21**, 193503, IOP Publishing, UK.)

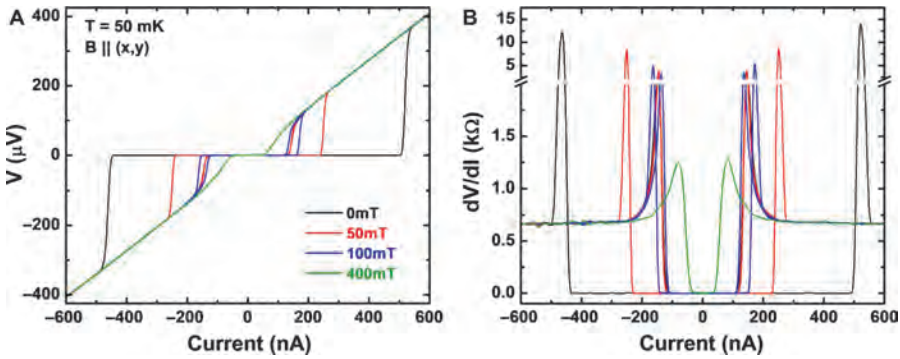


**Figure 16.9** *V–I* characteristics of a 500 nm wide wire at 50 mK under different magnetic fields applied in the plane of the sample, perpendicular to the current direction. A hysteretic behavior is seen until the field reaches 130 mT. Panel B shows the differential resistance extracted numerically from the *V–I* curves.

is due to vortex penetration in the devices. Here, the difference in the aspect ratio of the devices when applying the field parallel or perpendicular to the surface may result in a higher vortex density when the field is applied perpendicular to the sample surface. In the case of in-plane fields the measurements were done only until 400 mT and, for the 500 nm wide wire, we see a clear zero resistance state close to zero injection current even at the highest applied field.

In conclusion we have shown that nanofabricated samples made from boron-doped diamond retain their superconducting properties. We have also seen that larger grain sizes in the boron-doped diamond (BDD) film lead to more robust superconductivity with higher critical field and transition temperatures. Based on our findings on nanofabricated samples, we are in a position to fabricate and study quantum devices made from this material with larger grain sizes, which will be presented in the next section.

## 16.4 Superconducting Quantum Interference Device Made From Superconducting Diamond

As we have seen in the preceding section, superconductivity persists in nanoscale BDD samples and hence opens the possibility to realize superconducting devices with this very interesting material. The main idea is to explore the possibility of harnessing the high critical field of the material for making sensitive quantum devices, which can operate at magnetic fields of a few Teslas. Such a device is the superconducting quantum interference device (SQUID).

In this section we will describe the realization of a micron-scale superconducting quantum interference device (μ-SQUID). A SQUID is a superconducting loop containing one or more Josephson junctions and the

phase accumulated across the junctions results in a modulation of the critical current when an external magnetic field is applied. First invented by Jaklevic *et al.*,[25] it is an extremely sensitive device that can be used to measure extremely small magnetic fields. These devices find applications in various fields of science, such as scanning SQUID microscopy,[26,27] magnetoencephelography (MEG)[28] and magnetic property measurements,[27,29] to name a few.

A schematic of the measurement set-up for SQUID oscillations is presented in Figure 16.10. The SQUID is formed by a superconducting loop containing two weak links and is current-biased by adding a large biasing resistor $R_b$ in series with a voltage source $V_s$. The value of $R_b$ is chosen in such a way that $R_n$, the normal state resistance of the device, is much smaller than the biasing resistor. In our case with a normal state resistance of the order of a few kilo-ohms we chose 1 MΩ for the resistor such that the current in the circuit is determined by the biasing resistor at all times. To measure a *V–I* curve, we swept the source voltage and, therefore, the current in the circuit. We measured the output voltage with a low noise amplifier and recorded the bias current when the sample transited into its normal state. Such a measurement is repeated by varying the magnetic flux $\phi$ and the critical current shows a periodic behaviour as a function of the magnetic flux with the oscillation period being one flux quantum $\phi_o = h/2e$ in the SQUID loop, as shown schematically in panel B of Figure 16.10. Another way of measuring these oscillations is to bias the SQUID with a constant current close to $I_c$ and to measure the output voltage as a function of applied flux, although this technique is limited to shunted devices and will be discussed below. Now, if one biases the SQUID at the point of steepest slope (black point in panel B of Figure 16.10), a small change in flux through the SQUID loop results in a large change in the measured critical current. In this way this device acts as an extremely sensitive flux detector and, hence, a magnetic field detector capable of detecting fields as low as $10^{-14}$ T is

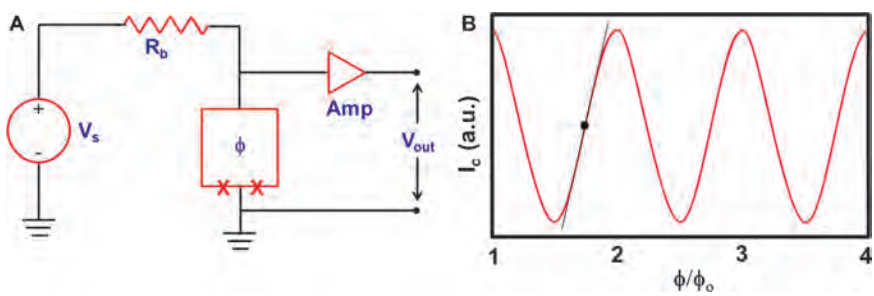


**Figure 16.10** Schematic of a SQUID showing a voltage source with a bias resistance $R_b$, which sets the current in the circuit. The crosses in the superconducting loop represent Josephson junctions. The critical current oscillation as a function of applied flux through the loop is schematically shown in panel B.

possible.[30,31] For comparison, the magnetic field of a heart is around $10^{-10}$ T and that of the human brain is around $10^{-13}$ T.

In general this detector has serious limitations in the form that it can only be used in environments where the magnetic field perpendicular to the SQUID plane is well below 1 T or by using a pick-up coil, which is placed within the magnetic field, while the SQUID has to be placed in a magnetic field protected environment.[29] In the literature one can find SQUIDs made from materials like $Nb_3Sn$[32] and $Nb_3Ge$,[33,34] which have high critical fields; however, their operation at high fields has not been proven to date. In the following subsection we will describe the study of μ-SQUIDs made from boron-doped diamond, which can be operated in magnetic fields in excess of 1 T. Such a device can find applications in the fields of ultrasensitive motion detection of nanomechanical systems[35] and high-field SQUID microscopy, to name a few.

### 16.4.1 Low Temperature Studies on Non-shunted Devices

Our μ-SQUID devices were fabricated out of 300 nm thick boron-doped diamond films using the steps depicted in Figure 16.1. A typical circuit, along with its components, is shown in Figure 16.11. Each circuit consists of six μ-SQUIDs—the difference being in the widths of the weak links, which in this case serve as the Josephson junctions.[36,37] We have fabricated devices with three different widths: 100 nm, 170 nm and 250 nm. The lengths of the links are kept fixed at 250 nm and the arms of the devices are 500 nm wide. The data presented here will be mostly from the μ-SQUID with weak links, a width of 100 nm and a length of 250 nm, unless otherwise stated. The area of the μ-SQUID is 2.5 μm×2.5 μm. The measurements were done in both a $^3$He close cycle refrigerator with a base temperature of 400 mK and a dilution refrigerator with a base temperature of 40 mK.

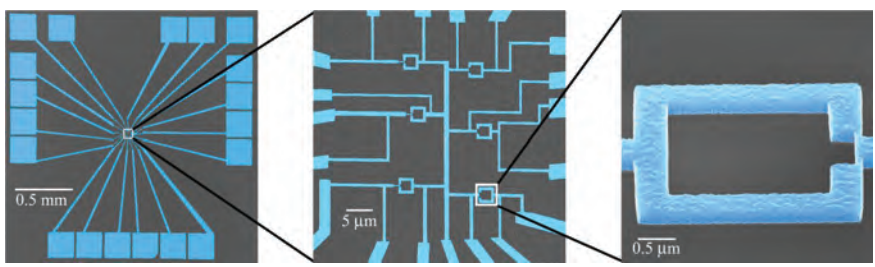


**Figure 16.11** Scanning electron micrographs of the μ-SQUID circuit. The left panel shows the complete circuit with several pads for ohmic contacts. The chip is 2 mm×2 mm in size. The middle panel shows the close-up view of a 50 μm×50 μm area in the middle of the sample. The right panel shows a tilted view of one of the μ-SQUIDs.
(Adapted with permission from Soumen Mandal *et al.* The Diamond Superconducting Quantum Interference Device, *ACS Nano*, 2011, **5**, 7144–7148, © 2011 American Chemical Society.)

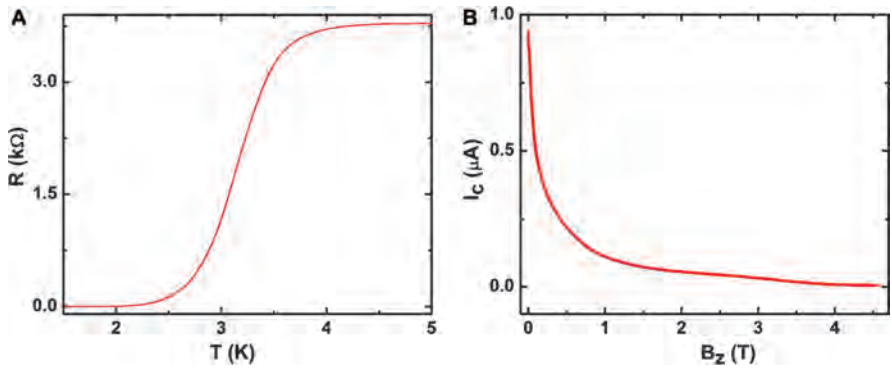


**Figure 16.12** Resistance *vs* temperature curve for our μ-SQUID showing a transition temperature of 3 K, which is also the transition temperature of the bulk wafer. Critical current as a function of out-of-plane magnetic field for a device with 100 nm wide weak link is shown in panel B. (Adapted with permission from Soumen Mandal *et al.* The Diamond Superconducting Quantum Interference Device, *ACS Nano*, 2011, **5**, 7144–7148, © 2011 American Chemical Society.)

We have performed detailed low-temperature characterizations of our devices.[38] In this subsection we will present the main results of our measurements. The resistance data from the measurements reveals a transition temperature of 3 K, as shown in panel A of Figure 16.12. The *V–I* characteristics of the samples were hysteretic but, on application of a magnetic field, the hysteresis disappeared once the critical current dropped below the re-trapping current due to pair-breaking effects. The hysteretic behavior is due to thermal effects.[24,39,40] The variation of the critical current with magnetic field is shown in panel B of Figure 16.12. The critical current drops exponentially until the field reaches 1 T and then the decay in the critical current is much slower until 4.5 T, where the sample is no longer superconducting. This existence of superconductivity at such high fields gives diamond the advantage of being a material for high field quantum devices.

We have also measured the critical current oscillation by applying the field both in-plane and out-of-plane.[38] A summary of the results is shown in Figure 16.13, where we present results from a μ-SQUID with 100 nm wide weak links. Panel A shows the oscillation at low fields, where the device is hysteretic. We see clear oscillations with a period of $\sim$0.31 mT, which corresponds to an effective area of the μ-SQUID of approximately $2.6 \times 2.6\ \mu m^2$, which is in agreement with our geometrical dimensions. The modulation amplitude is 15% for the device with 100 nm wide weak links, while our measurements for 170 nm wide weak links show a modulation of approximately 5%.[38] These modulation values are comparable to values seen in case of aluminium and niobium μ-SQUIDs.[41]

The sensitivity of our device can be estimated by repetitively measuring the critical current at a point of highest slope on the oscillation curve.

We obtained a sensitivity of $40\,\mu\Phi_o\ Hz^{-1/2}$, which is comparable to sensitivities of μ-SQUIDs with a similar design made from niobium and aluminium.[42] The sensitivity of the diamond μ-SQUID can be increased by carefully optimizing the SQUID design, as well as the material properties.[43] At present, the sensitivity is limited by our electronic setup, as well as external noise sources.

When a large magnetic field (>150 mT) is applied to the superconducting device, it reduces the critical current below the re-trapping current. This leads to a non-hysteretic nature of the voltage–current characteristic. Since the characteristic is non-hysteretic, an AC-based measurement technique can be used to record the SQUID oscillations. The measurement technique has been detailed in an earlier publication.[38]

We have measured voltage oscillations in our μ-SQUID at various magnetic fields up to 4 T. In panel B of Figure 16.13 we have shown the voltage

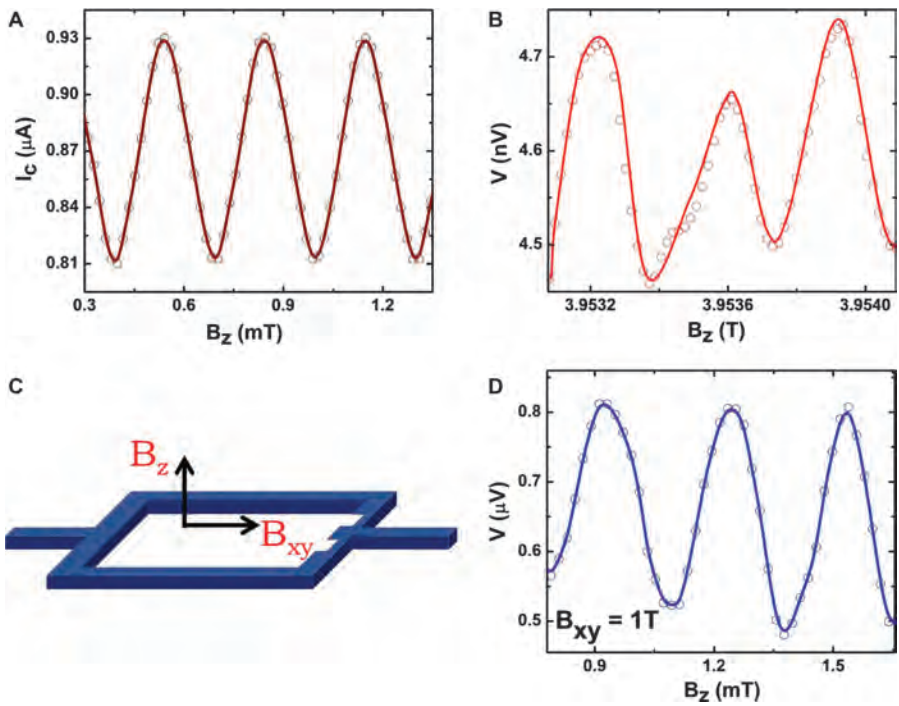


**Figure 16.13** Low field oscillations of the critical current for a μ-SQUID with 100 nm wide weak links are shown in panel A. The high field data for perpendicular field orientation ($B = B_z$) for the same device is shown in panel B. Panel D shows voltage oscillations for the parallel configuration ($B = B_{xy}$). The measurement configuration is shown schematically in panel C.
(Adapted with permission from Soumen Mandal *et al.* The Diamond Superconducting Quantum Interference Device, *ACS Nano*, 2011, **5**, 7144–7148, © 2011 American Chemical Society.)

oscillations close to 4 T. The periodicities of the oscillations are not perfectly symmetric. This is due to the fact that we are using the same coil with a field perpendicular to the μ-SQUID to apply a steady magnetic field up to 4 T, as well as the small variations of the order of 0.02 mT to probe the SQUID oscillations, which are of the order of 0.3 mT. Because of such small variations in the field, we measured the actual field values by averaging the value over a time scale of approximately 1 min. This limitation in the measurement setup can easily be removed by putting a feed line close to the μ-SQUID for probing the oscillations.[35]

We have also measured the voltage oscillations of our μ-SQUID by applying a constant field in the plane of the sample as schematized in panel C of Figure 16.13. The in-plane applied field, $B_{xy}$, is perpendicular to both weak links. A small probing field $B_z$ is applied perpendicular to the plane to measure the oscillations. In our measurements we have kept $B_{xy}$ constant at 0.5 T and 1 T, which is the highest possible field for our xy-coil and the result of the measurement with an in-plane field of 1 T is shown in panel D of Figure 16.13. The point worth mentioning here is that the thickness of our μ-SQUID is close to 300 nm, and in standard superconductors such oscillations are not visible under similar conditions when the layer thickness exceeds a few nanometers.[44]

In the literature one can find reports of extremely sensitive μ-SQUIDs being used in a variety of applications, like scanning SQUID microscopy,[26,42] magnetization measurements in mesoscopic systems[23,45] and in isolated molecules, to name a few.[46] However, a severe drawback of all these devices is the narrow range of magnetic fields that they can operate within. In addition, when μ-SQUIDs were operated at fields above 1 T, the field was applied perfectly in the plane of the sample,[44] keeping the thickness of the device close to few nanometers, which severely reduces the critical current of the system. The diamond μ-SQUID detailed in this section does not suffer from any such disability and can operate at fields as high as 4 T, as shown above, which is more than a six-fold increase over the present state of the art.[47]

### 16.4.2 First Trials on Shunted Devices

In the previous section we have shown that a μ-SQUID made from boron-doped diamond has functionality in applied fields in excess of 1 T; however, we have also found that its low field characteristics are hysteretic, which severely limits its usability with regards to measurement speed and sensitivity. Hence, it is important to see whether this hysteresis can be removed. As pointed out above, the hysteresis is mainly due to thermal effects and one way of removing the hysteresis is to put a heat shunt in contact with the weak links. In this way the heat generated by the device when it transits from the superconducting to the normal state can be evacuated instantaneously and the system will be void of any thermal effects.

For making shunted μ-SQUIDs, two different approaches can be considered. One possibility is to grow the diamond films on a metal surface, while the other is to cover the whole device with metal in the same way as ohmic contacts are made for measuring the devices. In this section we will show preliminary results using the first method. To choose an appropriate metal for the heat shunt, one has to consider the growth conditions. For a good quality diamond film, it is important that the diamond film sticks firmly to the substrate. For metal films, this adhesion is directly dependent on the ease with which the diamond film can form metal carbides. In this regard we chose tungsten, which readily forms carbide and thus gives rise to a good adhesion to the diamond film. To start with, we used two boron-doped diamond films grown on a tungsten film on a silicon wafer with different thicknesses of tungsten. The thickness of the tungsten layer was fixed at 20 nm and 50 nm. The steps for realizing the nano-circuits are the same as detailed in Figure 16.1. Only, in this case, the etching has to be done very carefully since the oxygen plasma also attacks the tungsten layer. We have made two circuits; one in which the tungsten layer has been left untouched and the other in which tungsten has been left only underneath the etched diamond layer, as shown schematically in Figure 16.14.

In this case the ohmic contacts were made by a silver paste instead of the usual titanium, platinum and gold trilayer. This is because the trilayer process requires 30 min baking in a high vacuum environment to generate the ohmic contact between the diamond and the metals. In order to avoid any diffusion of tungsten into the diamond layer this step was omitted. In Figure 16.15A and B we show scanning electron micrographs of the two types of circuit. Although the two sets of images look similar, on careful observation of the right panel in Figure 16.15B, one can identify a thin dark layer underneath the SQUID device, which corresponds to the tungsten layer left over after the etching process.

Here, μ-SQUID designs and dimensions are essentially the same as for our unshunted SQUIDs. The weak links have the same lengths (250 nm), while the width was varied from 100 to 170 and then to 250 nm. The different widths give rise to different critical currents of the system. In this section we will present data from the μ-SQUID with weak links of widths of 100 nm.

In the following we present the experimental results of a device with a shunt metal (50 nm of W) on the complete chip (panel A Figure 16.15), as


**Figure 16.14** Schematic of the two different circuits assessed for shunted SQUIDs. The blue layer is the silicon wafer, the red layer is tungsten (20 nm and 50 nm) and the green layer is boron-doped diamond (BDD).

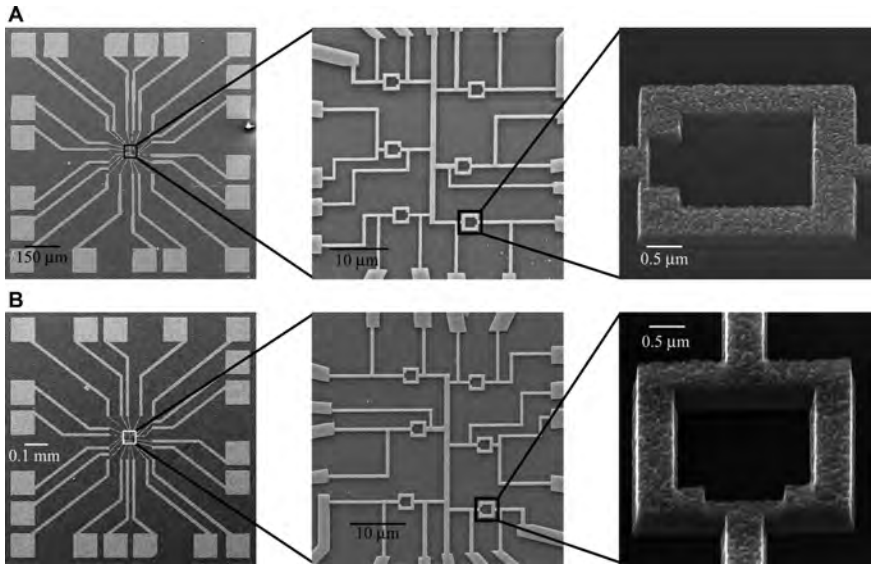


**Figure 16.15** A: SEM images of circuits with a full shunt layer underneath the SQUID. B: SEM image of the circuit with metal layer only under the diamond nanostructure. Note the thick dark layer underneath the structure in the right panel. This dark layer corresponds to the metal shunt.

shown in Figure 16.16. The resistance *versus* temperature curve shows two clear transitions. We associate the first transition, which is close to 1.2 K, to the weak links, while the other one is from the entire circuit and close to the bulk transition. We have measured the *V–I* characteristics of the device using the DC measurement technique, as previously described. The DC technique is particularly useful for checking the presence of hysteresis in the circuit. The *V–I* characteristic is S-shaped, which is typical for shunted superconducting devices and similar to what is observed for unshunted SQUIDs at high magnetic fields. The voltage oscillation can hence be measured with the same AC-measurement technique. We fix the bias current to 0.12 mA and record the resulting voltage oscillations as depicted in panel C of Figure 16.16.

To understand the behaviour of the shunt layer it is essential to understand the difference in critical current that we see in the case of non-shunted and shunted SQUIDs. For the shunted SQUID, we observe a critical current of 50 μA, which is significantly higher than what we have observed for non-shunted devices with similar dimensions, which have a value close to 1 μA. This, we believe, is due to the fact that the shunt layer covers the whole chip. When the diamond is in the superconducting state, all the current in the system passes through the diamond layer, but as soon as it reaches the normal state, the current in the system is divided between the shunt layer and the diamond layer. In this kind of geometry, when the diamond layer is

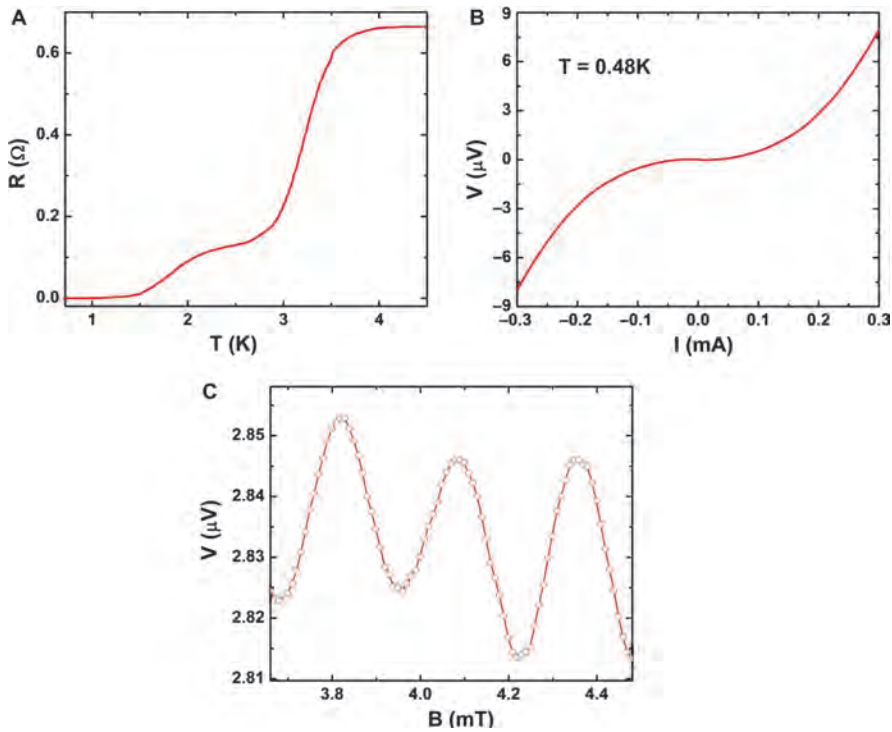


**Figure 16.16** Characteristics of a SQUID device with 100 nm wide weak links. The metal layer (50 nm W) under the circuit covers the whole chip area. Panel A shows the resistance *versus* temperature curve for the device. Two transitions are seen: one corresponding to the weak links and the other due to the rest of the circuit. The zero field *V–I* characteristics are shown in panel B. No hysteresis is seen in the curve. Panel C shows the low field voltage oscillation for the device when biased at a current of 0.12 mA.

in its normal state, there are many low resistance paths in the shunt for the current to flow, which are not only confined to the nanostructure. Since the resistance of the diamond layer is of the order of few kΩ and the shunt layer sheet resistance is close to 1 $\Omega\,\mathrm{sq}^{-1}$, a large portion of the current passes through the shunt layer and then the diamond layer transits back to the superconducting state. This leads to the increase in the critical current that we see. This argument is validated further by our results for the second set of samples, where the 50 nm shunt layer is geometrically confined below the nanostructure only. In that case a large increment in critical current ($I_c \sim 0.8$ μA) is not observed due to the higher resistance of the tungsten layer. Hence, a large current is needed in the case where the metal is spread over the entire chip to transit the diamond film into the normal state so that, even if the current is divided between the two layers, the current through the diamond layer is large enough to retain its normal state. For completeness,

let us add that, for films with a 20 nm thick tungsten shunt layer, the μ-SQUIDs were hysteretic for temperatures much below the transition temperature, and hence the shunt layer was not sufficient to evacuate the generated heat in the weak links.

In conclusion we have shown in the first part of this section that boron-doped diamond can be used to make sensitive quantum devices, which can be operated at very high magnetic fields. This opens up a variety of new application, such as their use with nanomechanical oscillators to fabricate sensitive motion detectors. Apart from that, we have also demonstrated that it is possible to build quantum devices void of any thermal effects using tungsten in contact with the nanostructure, improving its usability for low field applications. It is to be noted that further studies on device optimization with respect to an appropriate shunt layer thickness and shunt geometry is needed before final conclusions on the device capabilities can be drawn.

## 16.5 Nanomechanical Systems

In the preceding section we exploited the truly remarkable electric properties of boron-doped diamond and demonstrated that nanocrystalline boron-doped diamond is a promising material to realize superconducting quantum devices. In this section we would like to exploit the mechanical properties to show that boron-doped diamond can also find its application in the fields of micro- and nano-electromechanical systems.

More generally, nanomechanical resonators offer a wide range of applications in modern technology, as well as in state-of-the art research. On the one hand, they can be used as detectors for single atom masses,[48] single charges[49] and single spins.[50] On the other hand, an emerging class of highly miniaturized timing devices start to rival the electrical performance of the well-established quartz-based oscillators[51] that are used in modern technology. Applications range from real time tracking, frequency up and down conversion in radio frequency (RF) transceivers and the clocking of logical circuits.

The miniaturization of the resonators brings along a variety of new problems to the well-established field of micromechanical resonators.[52] A new set of transducers must be developed, surface properties start to play a significant role at submicron dimensions and it becomes more difficult to maintain a reproducible nanofabrication. Miniaturization, on the other hand, allows exploration of novel regimes, in particular the quantum regime.[53–55]

The challenge we address in the research presented here is the pursuit of high quality factors in nanomechanical systems. In a first approximation the quality factor describes the rate of energy loss compared to the energy stored in the resonator. An ideal dissipation-free resonator only vibrates at an infinitely narrow fundamental frequency with corresponding frequency harmonics, but since real systems are limited by interactions with their

surroundings, the oscillator is damped and its energy is dissipated. Electric-LC resonators, for example, exhibit quality factors that rarely surpass 100, while mechanical systems can exhibit very high quality factors up to several millions.[56–58]

Superconducting diamond is the perfect candidate for the realization of nanomechanical oscillators with very high quality factors. Its $sp^3$ hybridization, along with the resulting strong sigma bonds, make it the hardest material on Earth, resulting in a very high Young's modulus of the order of one terapascal.[59] In addition, its exceptional superconducting properties make it a perfectly dissipation-free system with regard to its electric properties. All energy loss is hence of a mechanical nature, which in turn should lead to extremely high quality factors. Furthermore, the high quality factor goes directly with a low energy exchange with the environment. Along with a high resonant frequency, this allows in principle the implementation of these kinds of structures in modern quantum information technology, for example, as tools for quantum metrology or as coupled hybrid quantum systems.

In the following we will present the first realization of BDD resonators. We will then introduce a simple experimental setup to detect and characterize nanomechanical resonators directly and will briefly underline the superb characteristics of superconducting diamond. An outline for future research aspects will be given at the end of this section.

In Figure 16.17 we present two nanomechanical BDD resonators. The fabrication process has already been detailed in Figure 16.1. We chose two different structures for our measurements: the first resonator consists only of boron-doped diamond to show that it is feasible to drive the resonator in its superconducting regime and the second resonator has a thin 50 nm gold layer on the top. This allows study of its behavior even at temperatures above the superconducting critical temperature, although these measurements will not be discussed here.

A well-established technique for measuring nanomechanical resonators is the so-called magneto-motive detection scheme.[60] It is mainly used to determine the characteristic properties of a resonator, such as its resonance frequency, non-linear behavior and its quality factor. In addition, this technique allows one to distinguish a mechanical resonance from an electrical one by simply varying the magnetic field. When an oscillating current

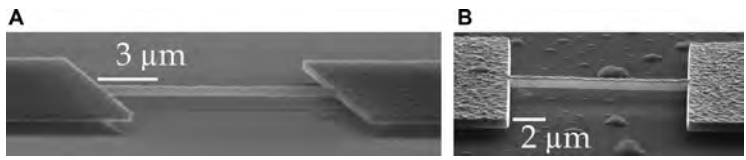


**Figure 16.17** BDD nanomechanical resonator. Panel A shows a pure BDD resonator with dimensions 12 μm×300 nm×325 nm (length×width×thickness), whereas panel B shows a BDD resonator with a thin gold layer on the top. Its dimensions are 12 μm×500 nm×(325 + 50) nm.

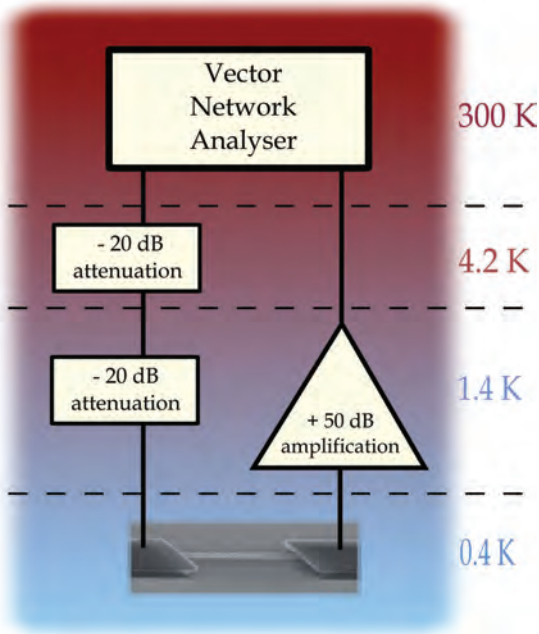


**Figure 16.18** Schematic of the experimental cryogenic setup. The sample is actuated with an AC-signal from the vector network analyzer and actuated *via* the Lorentz force in a magnetic field at low temperatures.

is passed through the resonator in a magnetic field perpendicular to the current flow, the resonator is actuated *via* the Lorentz force when the driving frequency matches the resonance frequency of the structure. At the same time, the motion of the oscillator induces a time-varying voltage due to Faraday's law, which manifests itself as an increase of the impedance of the device. In our setup this impedance is measured *via* a transmission measurement, which is carried out using a Rhode and Schwartz vector network analyzer (VNA), as depicted in Figure 16.18.

The signal from the generator port is fed through a 50 Ω adapted coaxial line with two cryogenic attenuation stages. The first thermalization takes place at the 4.2 K stage, the second at the 1.2 K stage with two identical attenuators of 20 dB each. The signal is then fed through the sample that is located at the lowest temperature stage of the $^3$He cryostat with a base temperature of 400 mK. The transmitted signal is amplified with a commercial low noise amplifier (Caltech CITLF1 SN120) that is thermally anchored at 4.2 K and recorded *via* the input port of the VNA, which measures the amplitude, as well as the phase of the signal. All measurements were carried out using this setup.

The transmission has been measured as a function of input power and external magnetic field in order to identify the superconducting–normal transition of the mechanical resonator. Figure 16.19 shows this behavior for

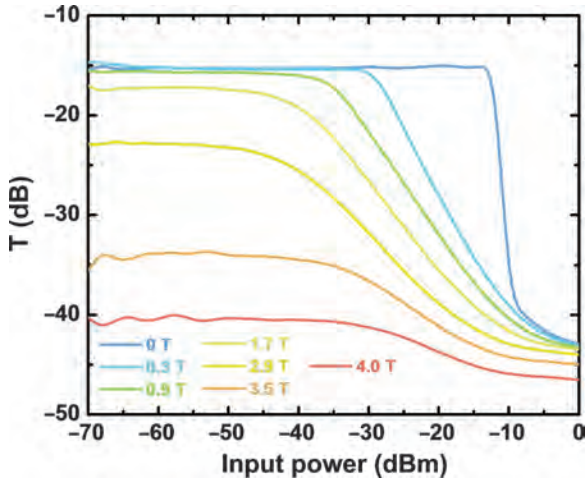


**Figure 16.19** Transmission through the sample for different input powers at different magnetic fields. The x-axis shows the input power and the transmission is plotted along the y-axis.

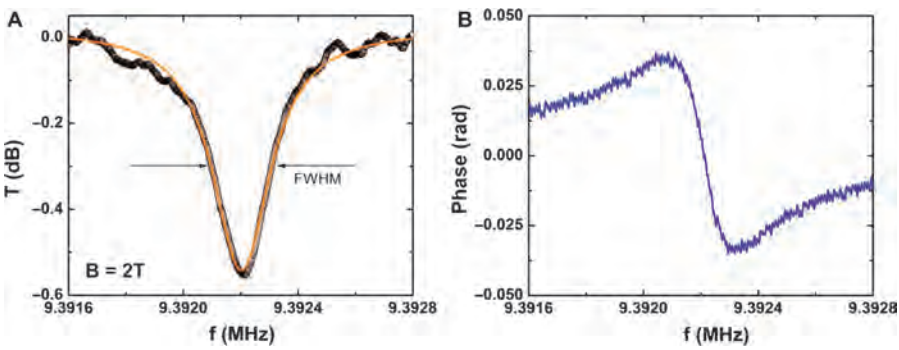


**Figure 16.20** A: the transmitted signal at resonance of the pure diamond resonator at a magnetic field of 2 T. B: the phase response. The full-width at half-maximum (FWHM) is indicated for the calculation of the quality factor.

the pure diamond beam from Figure 16.17. At zero magnetic field (blue curve), one can clearly identify the superconducting state: the transmitted signal is constant up to $-10$ dBm input power.

At this point, the superconducting-to-normal-state transition occurs and the transmission drops about 27 dB. From this value we can calculate the series resistance of the device to be approximately $\sim 2.1$ kΩ, which corresponds to the normal state resistance of the mechanical resonator. The transition occurs at lower input power for higher magnetic field until about a magnetic field of 4 T, above which the sample stays normal.

In Figure 16.20 we present the mechanical properties of the resonator, where we measure the frequency response of our oscillator. Panel A in

Figure 16.20 depicts the transmitted signal at resonance at a magnetic field of 2 T. From a Lorentzian fit we can extract the loaded quality factor of about 40000 and, from the phase response (panel B), we determine the exact resonance frequency to be 9.392110 MHz (zero crossing of the phase). The quality factor in our system is mainly limited by clamping and surface losses due to the strong undercut of the clamping pads by the HF etching procedure, as seen in Figure 16.17. Further measurements are, however, necessary to confirm this statement. The loss mechanism can, in principle, be studied *via* the length dependence of the quality factor in greater detail.[61]

One disadvantage of the magneto-motive detection scheme is the onset of eddy currents inside the structure, which gives rise to an additional magnetic field that is opposed to the applied external magnetic field. This leads to an additional force acting on the resonator that is opposite to its movement. This additional damping adds linearly to the intrinsic mechanical damping, whereas its contribution is quadratic as depicted in Figure 16.21. From the fit we can extract the unloaded or intrinsic quality factor of about 41000.

In order to compare to other nanomechanical resonators made from different materials, it is common to calculate the product of resonance frequency and quality factor for which we obtain $3.37\times10^{11}$. This value is similar to state-of-the-art mechanical resonators.[62]

The ability to realize superconducting diamond resonators has a variety of possible applications in modern research. Their mechanical and superconducting properties make them an outstanding candidate for the integration into superconducting quantum circuits. It is feasible to incorporate such a high quality resonator into a SQUID loop[35] or to couple it to a superconducting cavity[63] for ultrasensitive displacement detection.

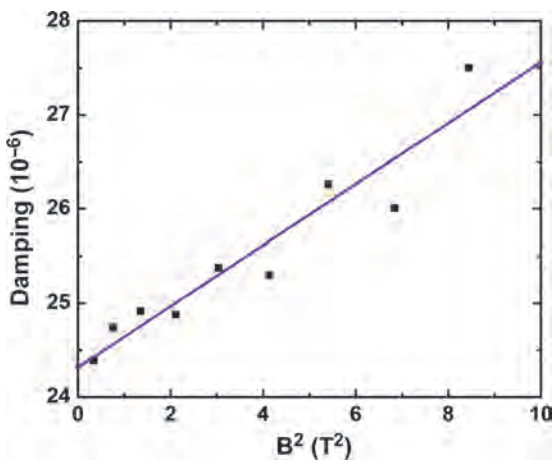


**Figure 16.21** Eddy current damping as a function of the square of the magnetic field. The intrinsic mechanical damping can be extracted by extrapolation to zero magnetic field.

## 16.6 Summary and Conclusions

In conclusion we have presented in this chapter a comprehensive study on nanostructures made from boron-doped diamond. It has been shown that the material retains its remarkable properties even when it is nanofabricated. We have also demonstrated the working of a micron-sized SQUID made from boron-doped diamond. SQUIDs made from boron-doped diamond retain their functionality even at fields as high as 4 T. We have also attempted to make shunted devices out of this material but rigorous efforts are needed before realizing a device that can be usefully employed in various applications. Lastly, we have presented our results from nanomechanical resonators, which clearly show that this material is indeed a good candidate for making monolithic superconducting nanomechanical devices. The next steps in realizing better devices can be divided into two parts: a first approach can be to investigate various design parameters to obtain the best sensitivity and quality factors. A second approach can address the material considerations, which may lead to nanocrystalline samples with higher critical parameters, like critical temperature, critical field, Young's modulus *etc.* In particular, boron-doped diamond grown on substrates to induce compressive stress in the diamond layer would significantly enhance the quality factor.[64–67] It also remains to be seen what happens when these devices are made from monocrystalline diamond films. It is expected that the monocrystalline films may result in better devices due to the absence of inherent defects, like grain boundaries and $sp^2$ carbon present in the nanocrystalline BDD films; however, the fabrication and measurement techniques may have to be adapted for handling monocrystalline diamond-based devices.

## Acknowledgement

We would like to acknowledge technical assistance from the Nanofab team of the Institut Néel, in particular B. Fernandez. We also acknowledge valuable discussions and help from Y. Baines, V. Bouchiat, E. Bustarret, K. Hasselbach, T. Meunier, C. Naud, F. Omnes, L. Saminadayar, W. Wernsdorfer and O. Williams. This work has been supported by the French National Funding Agency (ANR) in the frame of its program in ''Nanosciences and Nanotechnologies'' (SUPERNEMS Project no. ANR-08-NANO-033).

## References

1. H. T. Hall, *Science*, 1958, **128**, 445–449.
2. M. Werner and R. Locher, *Reports on Progress in Physics*, 1998, **61**, 1665.
3. M. C. Costello, D. A. Tossell, D. M. Reece, C. J. Brierley and J. A. Savage, *Diamond and Related Materials*, 1994, **3**, 1137–1141.
4. E. A. Ekimov, V. A. Sidorov, E. D. Bauer, N. N. Mel'nik, N. J. Curro, J. D. Thompson and S. M. Stishov, *Nature*, 2004, **428**, 542–545.

5. X. Blase, E. Bustarret, C. Chapelier, T. Klein and C. Marcenat, *Nat Mater*, 2009, **8**, 375–382.
6. G. Dubitskiy, V. Blank, S. Buga, E. Semenova, V. Kul'bachinskii, A. Krechetov and V. Kytin, *JETP Letters*, 2005, **81**, 260–263.
7. M. Nesladek, D. Tromson, C. Mer, P. Bergonzo, P. Hubik and J. J. Mares, *Applied Physics Letters*, 2006, **88**, 232111.
8. W. Gajewski, P. Achatz, O. A. Williams, K. Haenen, E. Bustarret, M. Stutzmann and J. A. Garrido, *Physical Review B*, 2009, **79**, 045206.
9. P. Achatz, W. Gajewski, E. Bustarret, C. Marcenat, R. Piquerel, C. Chapelier, T. Dubouchet, O. A. Williams, K. Haenen, J. A. Garrido and M. Stutzmann, *Physical Review B*, 2009, **79**, 201203.
10. M. Imboden, P. Mohanty, A. Gaidarzhy, J. Rankin and B. W. Sheldon, *Applied Physics Letters*, 2007, **90**, 173502.
11. A. Gaidarzhy, M. Imboden, P. Mohanty, J. Rankin and B. W. Sheldon, *Applied Physics Letters*, 2007, **91**, 203503–203503.
12. M. Imboden and P. Mohanty, *Physical Review B*, 2009, **79**, 125424.
13. Y. Takano, *Journal of Physics: Condensed Matter*, 2009, **21**, 253201.
14. J. Bardeen, L. N. Cooper and J. R. Schrieffer, *Physical Review*, 1957, **106**, 162–164.
15. G. Baskaran, *Science and Technology of Advanced Materials*, 2008, **9**, 044104.
16. J. J. Mareš, P. Hubik, J. Krištofik and M. Nesládek, *Science and Technology of Advanced Materials*, 2008, **9**, 044101.
17. E. A. Ekimov, V. A. Sidorov, A. V. Zoteev, J. B. Lebed, J. D. Thompson and S. M. Stishov, *Science and Technology of Advanced Materials*, 2008, **9**, 044210.
18. O. A. Williams, O. Douhéret, M. Daenen, K. Haenen, E. Ōsawa and M. Takahashi, *Chemical Physics Letters*, 2007, **445**, 255–258.
19. O. A. Williams, M. Nesladek, M. Daenen, S. Michaelson, A. Hoffman, E. Osawa, K. Haenen and R. B. Jackman, *Diamond and Related Materials*, 2008, **17**, 1080–1088.
20. O. A. Williams, *Diamond and Related Materials*, 2011, **20**, 621–640.
21. S. Mandal, C. Naud, O. A. Williams, É. Bustarret, F. Omnès, P. Rodière, T. Meunier, L. Saminadayar and C. Bäuerle, *Nanotechnology*, 2010, **21**, 195303.
22. S. Mandal, C. Naud, O. A. Williams, É. Bustarret, F. Omnès, P. Rodière, T. Meunier, L. Saminadayar and C. Bäuerle, *Physica Status Solidi (a)*, 2010, **207**, 2017–2022.
23. W. Rabaud, L. Saminadayar, D. Mailly, K. Hasselbach, A. Benoît and B. Etienne, *Physical Review Letters*, 2001, **86**, 3124–3127.
24. H. Courtois, M. Meschke, J. T. Peltonen and J. P. Pekola, *Physical Review Letters*, 2008, **101**, 067002.
25. R. C. Jaklevic, J. Lambe, A. H. Silver and J. E. Mercereau, *Physical Review Letters*, 1964, **12**, 159–160.
26. J. R. Kirtley, C. C. Tsuei, J. Z. Sun, C. C. Chi, L. S. Yu-Jahnes, A. Gupta, M. Rupp and M. B. Ketchen, *Nature*, 1995, **373**, 225–228.

27. R. C. Black and F. C. Wellstood, in *The SQUID Handbook*, eds. J. Clarke and A. I. Braginski, WILEY-VCH Verlag GmbH & Co. KGaA, Weinheim, 2006, vol. 2, pp. 392–436.
28. D. Cohen, *Science*, 1972, **175**, 664–666.
29. R. Kleiner, D. Koelle, F. Ludwig and J. Clarke, *Proceedings of the IEEE*, 2004, **92**, 1534–1548.
30. J. Vrba, J. Nenonen and L. Trahms, in *The SQUID Handbook*, eds. J. Clarke and A. I. Braginski, WILEY-VCH Verlag GmbH & Co. KGaA, Weinheim, 2006, vol. 2, pp. 299–300.
31. M. B. Ketchen, W. M. Goubau, J. Clarke and G. B. Donaldson, *Journal of Applied Physics*, 1978, **49**, 4111–4116.
32. C. T. Wu and C. M. Falco, *Applied Physics Letters*, 1977, **30**, 609–611.
33. H. Rogalla, B. David and J. Ruhl, *Journal of Applied Physics*, 1984, **55**, 3441–3443.
34. M. Dilorio, A. de Lozanne and M. Beasley, *Magnetics, IEEE Transactions on*, 1983, **19**, 308–311.
35. S. Etaki, M. Poot, I. Mahboob, K. Onomitsu, H. Yamaguchi and H. S. J. van der Zant, *Nat Phys*, 2008, **4**, 785–788.
36. P. W. Anderson and A. H. Dayem, *Physical Review Letters*, 1964, **13**, 195–197.
37. K. K. Likharev, *Reviews of Modern Physics*, 1979, **51**, 101–159.
38. S. Mandal, T. Bautze, O. A. Williams, C. Naud, É. Bustarret, F. Omnès, P. Rodière, T. Meunier, C. Bäuerle and L. Saminadayar, *ACS Nano*, 2011, **5**, 7144–7148.
39. W. J. Skocpol, *Physical Review B*, 1976, **14**, 1045–1051.
40. D. Hazra, L. M. A. Pascal, H. Courtois and A. K. Gupta, *Physical Review B*, 2010, **82**, 184530.
41. K. Hasselbach, D. Mailly and J. R. Kirtley, *Journal of Applied Physics*, 2002, **91**, 4432–4437.
42. K. Hasselbach, C. Veauvy and D. Mailly, *Physica C: Superconductivity*, 2000, **332**, 140–147.
43. R. Voss, R. Laibowitz, A. Broers, S. Raider, C. Knoedler and J. Viggiano, *IEEE Transactions on Magnetics*, 1981, **17**, 395–399.
44. L. Chen, W. Wernsdorfer, C. Lampropoulos, G. Christou and I. Chiorescu, *Nanotechnology*, 2010, **21**, 405504.
45. H. Bluhm, N. C. Koshnick, J. A. Bert, M. E. Huber and K. A. Moler, *Physical Review Letters*, 2009, **102**, 136802.
46. W. Wernsdorfer and R. Sessoli, *Science*, 1999, **284**, 133–135.
47. A. Finkler, Y. Segev, Y. Myasoedov, M. L. Rappaport, L. Ne'eman, D. Vasyukov, E. Zeldov, M. E. Huber, J. Martin and A. Yacoby, *Nano Letters*, 2010, **10**, 1046–1049.
48. K. Jensen, K. Kim and A. Zettl, *Nat Nano*, 2008, **3**, 533–537.
49. G. A. Steele, A. K. Hüttel, B. Witkamp, M. Poot, H. B. Meerwaldt, L. P. Kouwenhoven and H. S. J. van der Zant, *Science*, 2009, **325**, 1103–1107.
50. D. Rugar, R. Budakian, H. J. Mamin and B. W. Chui, *Nature*, 2004, **430**, 329–332.

51. J. T. M. van Beek and R. Puers, *Journal of Micromechanics and Microengineering*, 2012, **22**, 013001.
52. K. L. Ekinci and M. L. Roukes, *Review of Scientific Instruments*, 2005, **76**, 061101.
53. J. Chan, T. P. M. Alegre, A. H. Safavi-Naeini, J. T. Hill, A. Krause, S. Groblacher, M. Aspelmeyer and O. Painter, *Nature*, 2011, **478**, 89–92.
54. J. D. Teufel, T. Donner, D. Li, J. W. Harlow, M. S. Allman, K. Cicak, A. J. Sirois, J. D. Whittaker, K. W. Lehnert and R. W. Simmonds, *Nature*, 2011, **475**, 359–363.
55. A. D. O'Connell, M. Hofheinz, M. Ansmann, R. C. Bialczak, M. Lenander, E. Lucero, M. Neeley, D. Sank, H. Wang, M. Weides, J. Wenner, J. M. Martinis and A. N. Cleland, *Nature*, 2010, **464**, 697–703.
56. J. E.-Y. Lee and A. A. Seshia, 5.4-MHz single-crystal silicon wine glass mode disk resonator with quality factor of 2 million, *Sensors and Actuators A: Physical*, 2009, **156**(1), 28–35.
57. A. K. Hüttel, G. A. Steele, B. Witkamp, M. Poot, L. P. Kouwenhoven and H. S. J. van der Zant, *Nano Letters*, 2009, **9**, 2547–2552.
58. E. A. Laird, F. Pei, W. Tang, G. A. Steele and L. P. Kouwenhoven, *Nano Letters*, 2011, **12**, 193–197.
59. O. A. Williams, A. Kriele, J. Hees, M. Wolfer, W. Müller-Sebert and C. E. Nebel, *Chemical Physics Letters*, 2010, **495**, 84–89.
60. M. Poot and H. S. J. van der Zant, *Physics Reports*, 2012, **511**, 273–335.
61. X. M. H. Huang, X. L. Feng, C. A. Zorman, M. Mehregany and M. L. Roukes, *New Journal of Physics*, 2005, **7**, 247.
62. D. R. Schmid, P. L. Stiller, C. Strunk and A. K. Hüttel, *New Journal of Physics*, 2012, **14**, 083024.
63. C. A. Regal, J. D. Teufel and K. W. Lehnert, *Nat Phys*, 2008, **4**, 555–560.
64. S. S. Verbridge, J. M. Parpia, R. B. Reichenbach, L. M. Bellan and H. G. Craighead, *Journal of Applied Physics*, 2006, **99**, 124304–124308.
65. Q. P. Unterreithmeier, T. Faust and J. P. Kotthaus, *Physical Review Letters*, 2010, **105**, 027205.
66. T. Faust, P. Krenn, S. Manus, J. P. Kotthaus and E. M. Weig, *Nat Commun*, 2012, **3**, 728.
67. J. Rieger, T. Faust, M. J. Seitner, J. P. Kotthaus and E. M. Weig, *Applied Physics Letters*, 2012, **101**, 103110–103114.